Journal of Industrial and Engineering Chemistry 71 (2019) 137–149

Contents lists available at ScienceDirect

Journal of Industrial and Engineering Chemistry

journal homepage: www.elsevier.com/locate/jiec

Structural optimization in the same polymer backbones for efficient polymer solar cells: Relationship between steric hindrance and molecular weight

Sung Jae Jeon, Jeong Eun Yu, Yong Woon Han, Il Soon Suh, Doo Kyung Moon*

Nano and Information Materials (NIMs) Laboratory, Department of Chemistry Engineering, Konkuk University, 120, Neungdong-ro, Gwangjin-gu, Seoul 05029, Republic of Korea

ARTICLE INFO

Article history:
Received 10 October 2018
Received in revised form 22 October 2018
Accepted 10 November 2018
Available online 16 November 2018

Keywords:
Polymer solar cells
D–A conjugated polymers
Computational simulation
Dihedral angles

ABSTRACT

Structural optimization by using donor–acceptor (D–A) conjugated polymers is a promising strategy for improving the power conversion efficiencies (PCEs) of polymer solar cells (PSCs). In this study, we report the best PCE of 8.9% based on $PC_{71}BM$ that was achieved by using a 250 nm thick active layer in an inverted device through the optimization of side chains of P(2DBDT-DTffBT) backbones. Specifically, by varying the alkyl side chain lengths and shapes in the acceptor unit of polymers, the effect of side chain engineering on photovoltaic performance was systematically studied in terms of the relationship between steric hindrance and molecular weight.

Introduction

PSCs[1] with a BHJ structure have been regarded as next-generation solar cells owing to their advantages of low cost, light weight, solution processability, mechanical flexibility, and short energy payback time [1–3]. The state-of-the-art PCEs of single-junction BHJ PSCs have been reported to be above 11% for PSCs based on fullerene derivatives, especially, more than 13% for non-fullerene PSCs, owing to the major efforts involved in developing new organic materials and optimizing device structures [5–22]. However, despite their many advantages and increased efficiencies, PSCs need to be improved in many aspects before they can be commercialized; these include an easier solution process, manufacturing cost reduction, thickness control of the photoactive layer, module stability, *etc.* [23]. In particular, to obtain high-performance and low-cost PSCs, issues such as a complex solution process and high manufacturing costs should be overcome [24]. Furthermore, most PSC-based BHJ photoactive layer systems are reported to show the best performance for 80–100 nm thickness [3,25]. Owing to this change in performance according to thickness, it is difficult to reproducibly fabricate uniform large-area films without defects, as required for PSC commercialization; high sensitivity and roll-to-roll manufacturing are required in the future [26,27]. As stated, the design of the photoactive layer material and process feasibility are becoming more important for commercialization.

Many studies over the years have emphasized that side chain engineering can affect the properties of D–A conjugated polymers [28–32]. Consequently, their electrical conductivity, charge carrier mobility, and PCE are affected [33]. Uniform alkyl side chain arrangements can promote side chain interchain interdigitation and increase the degree of lamellar ordering and the packing of main backbones, which ultimately can result in D–A conjugated polymer-based organic electronics exhibiting high performances [34–38]. In addition, rather than developing new D–A conjugated building blocks, it can be more convenient and cost-effective to modify the alkyl side chains of the high-performance D–A polymer backbones, as presented in many reports [39–41].

However, predicting which alkyl side chain is best is still difficult and is specific to individual polymer backbones [42–44].

* Corresponding author.
E-mail address: dkmoon@konkuk.ac.kr (D.K. Moon).

[1] Polymer solar cells (PSCs); bulk heterojunction (BHJ); power conversion efficiencies (PCEs); donor–acceptor (D–A); benzodithiophene (BDT); benzothiadiazole (BT); two-dimensional benzodithiophene (2DBDT); naphthobisthiadiazole (NBT); dithienyldifluoroBT (DTffBT); highest occupied molecular orbital (HOMO); diphenyl ether (DPE); [6,6]-phenyl C_{71} butyric acid methyl-ester ($PC_{71}BM$); elemental analysis (EA); photoluminescence (PL); cyclic voltammetry (CV); indium tin oxide (ITO); thermogravimetric analysis (TGA); differential scanning calorimetry (DSC); gel permeation chromatography (GPC); X-ray diffraction (XRD); atomic force microscopy (AFM); density functional theory (DFT); zinc oxide (ZnO); poly[(9,9-bis(3'-(*N*,*N*-dimethylamino)propyl)-2,7-fluorene)-alt-2,7-(9,9–dioctylfluorene)] (PFN); polytetrafluoroethylene (PTFE); chlorobenzene (CB); transition state (TS); lowest unoccupied molecular orbital (LUMO); intramolecular charge transfer (ICT); fill factor (FF); external quantum efficiency (EQE); root-mean-square roughness (RMS); space charge limited current (SCLC).

https://doi.org/10.1016/j.jiec.2018.11.016
1226-086X/

We previously reported the changes in molecular structure and performance during the design of D–A type conjugated polymers according to the type and position of the side chains [45,46]. With respect to the modification of alkyl side chain lengths and shapes, Janssen et al. reported that the long linear alkyl chains of BDT-BT polymers, despite improving the solubility, caused a decrease in the PCE due to increased bimolecular recombinations [47–49]. In addition, Prof. Yang groups characterized the changes in polymer crystallinity and film morphology through the substitution of linear or branched alkyl side chains in the thiophene spacer, which links the 2DBDT and NBT polymer main backbones. They reported a maximum PCE of above 8% with a 250 nm thick layer [50]. As seen from those studies, side chain engineering of D–A polymer backbones that balances solubility and crystallinity is key to obtaining an optimal BHJ morphology with high performance.

In this study, to examine the effects of side chain engineering between the D and the A in more detail, we designed and synthesized DTffBT-based polymers with different side chains. As a D unit, 2DBDT was used during the polymer design, which is a popular electron-donating building block that exhibits high performance [51]. In particular, because 2DBDT has an extended conjugation length towards the 4,8 positions of BDT, as well as a more rigid and large coplanar structure, it has the advantage of enhanced π–π stacking between adjacent polymer backbones [52,53]. Moreover, because 2DBDT has a symmetric structure with regioregularity, it can display high compatibility with various acceptor units and a high degree of polymerization [52,54,55]. As an A unit, ffBT was used, which has superior electron-withdrawing property and good compaction characteristics [56]. ffBT has two fluorine atoms, which lower the HOMO level to below that of BT; this leads to stronger non-covalent interaction between adjacent molecules, resulting in higher planarity [57]. In particular, by introducing two variable alkyl side chain-substituted thiophene spacers (DT) on both sides of the 4,7 positions of ffBT, this study explored the optimized structure of P(2DBDT-DTffBT) backbones [58]. The 2DBDT and DTffBT units used for polymerization are well known for their ease of synthesis and purification, therefore, these materials are promising for large-scale manufacturing [52,59,60].

Through side chain engineering of the thiophene spacers between the D and the A, conjugated polymers (P-Cn, where n: the number of alkyl side chain carbons attached to thiophene) were synthesized with linear (butyl, hexyl, octyl) and branched (ethyl hexyl) alkyl chains; the corresponding polymers were named P-C4, P-C6, PC8, and PC2C6, respectively. The polymers showed varied synthesizing behaviors and packing patterns depending on the types of alkyl side chains, which could also influence the physical, optical, and electrical properties of the polymers. Interestingly, we discovered that the degree of polymerization and the molecular packing properties of 2DBDT-DTffBT-based polymers tended to become lower as the lengths of the side chains increased and the shape changed from linear-type to branched-type. This was systemically analyzed through computational simulation, and it was found that it is related to the steric hindrance caused by the change in the side chains of the thiophene spacer introduced between the D and the A. This has been summarized in Chart 1 .

Finally, for PSC studies, employing small amounts of DPE as the processing additive, the butyl side chain-substituted P-C4 blended with $PC_{71}BM$ was found to yield PCEs approaching 9% at the active layer thickness of 250 nm, which represents a significant improvement over their much longer linear and branched alkyl chain-substituted counterparts, for which the PCEs are lower than 7% (in fact, the fabrication of P-C2C6 was impossible). Our results indicated that the side chain engineering of D–A type polymers promotes the design of high-performance polymers through the formation of ordered microstructures and interpenetrating networks with $PC_{71}BM$, which accelerate charge carrier transport. This report is expected to offer interesting information regarding the molecular design of D–A polymers.

Experimental

Instruments and characterization

Unless otherwise specified, all reactions were performed under nitrogen atmosphere. The solvents were dried using standard procedures. All column chromatography was performed with silica

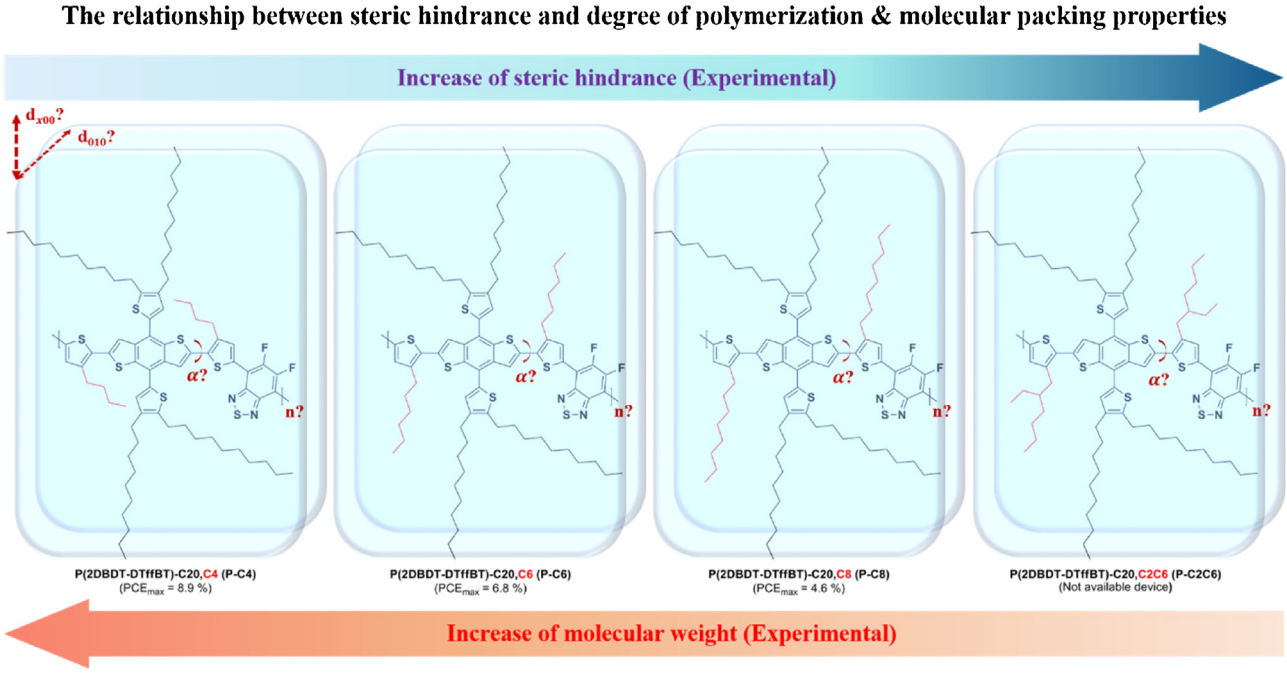

Chart 1. Schematic and description in this study.

gel (230–400 mesh, Merck) as the stationary phase. A microwave reactor (Biotage Initiator^{+}) was used to synthesize the polymers. ^{1}H NMR spectra were collected by using a Bruker ARX 400 spectrometer with $CDCl_3$ solution, the chemical concentration of which was recorded in parts per million using TMS as the internal standard. EA was performed with a Thermofinigan EA2000. The UV absorption and PL spectra were measured in chloroform using a HP Agilent 8453 UV–vis spectrophotometer and Perkin Elmer LS55, respectively. CV curves were obtained by using a Zahner IM6eX electrochemical workstation, with 0.1 M acetonitrile solution (purged with nitrogen for 20 min) containing tetrabutyl ammonium hexafluorophosphate (Bu_4NPF_6) as the electrolyte, at the constant scan rate of 50 mV/s. ITO, a Pt wire, and silver/silver chloride [Ag in 0.1 M KCl] were used as the working, counter, and reference electrodes, respectively. The electrochemical potential was calibrated against Fc/Fc+. The HOMO levels of the polymers were determined using the oxidation onset potential. The onset potentials are the values obtained from the intersection of the two tangents drawn at the points of increasing current and changing baseline current of the CV curves. TGA measurements were performed by using a NETZSCH TG 209 F3 thermogravimetric analyzer. DSC measurements were carried out with NETZSCH DSC 200 F3 in the temperature range 30–300 °C. All GPC analyses were performed using chloroform as the eluent and a polystyrene standard as the reference. XRD patterns were obtained using a Smart Lab 3 kW (40 kV, 30 mA, Cu target, wavelength: 1.541871 Å) instrument manufactured by Rigaku, Japan. Topographic images of the active layers were obtained through AFM in the tapping mode under ambient conditions by using an XE-100 instrument. The optimized molecular geometries of the model molecules were obtained by minimizing the energy through calculations using the Gaussian 09 software. Theoretical analyses were performed based on DFT and dihedral angle scans that were approximated by using the B3LYP functional and 6-31G(d) basis set.

Fabrication and characterization of PSCs

All the BHJ photovoltaic cells were prepared by using the following device fabrication procedure. ITO glass (10 Ω/sq, Samsung corning) was sequentially sonicated in detergent (Alconox in deionized water, 10%), acetone, isopropyl alcohol, and deionized water for 20 min. Moisture was thoroughly removed with N_2 gas flow. To ensure complete removal of the remaining water, the ITO glass was heated on a hot plate for 10 min at 100 °C. For hydrophilic treatment of the ITO glass surface, the glass was cleaned for 10 min in an UVO cleaner, and ZnO or a hybrid type of ZnO with PFN was passed through a 0.45 μm PTFE filter before being deposited onto the ITO glass to produce a 40 nm thick layer by spin-coating at 4000 rpm. The coated glass was then dried at 150 °C for 1 h in air. Composite 1.5 wt% solutions of the polymers and $PC_{71}BM$ were prepared by using CB with 3.0% DPE for 20 min at 90 °C. The solutions were filtered using the 0.45 μm PTFE filter and then spin-coated (700–4000 rpm, 30 s) on top of the ZnO layer in high purity of nitrogen filled glove box. The fabrication of the inverted device was completed by depositing thin layers of ZnO (or ZnO + PFN; ~40 nm), MoO_3 (2 nm), and Ag (100 nm) at pressures less than 1026 Pa. The active area of the device was 0.04–0.12 cm^2. Finally, the cell was encapsulated using an UV-curing glue (Nagase, Japan). The output photocurrent was adjusted to match the photocurrent of the Si reference cell to obtain a power density of 100 mW cm^{-2}. After encapsulation, all the devices were operated under ambient atmosphere.

Polymerization

Scheme 1 outlines the synthetic route to the monomers and polymers. The detailed synthetic procedures and characterization results for the monomers (A1, A2, A3, A4, and D1) and polymers (**P-C4**, **P-C6**, **P-C8,** and **P-C2C6**) are presented in Supporting Information (SI; Fig. S1 to S9).

P(2DBDT-DTffBT)-C20, CmCn (m/n = 4/0, 6/0, 8/0, 2/6), (P-C4, P-C6, P-C8, and P-C2C6)

To a mixture of the monomer A1 (or A2, A3, A4; 0.1 mmol), D1 (123.5 mg, 0.0995 mmol), tris(dibenzylideneacetone)dipalladium (0) (1.8 mg, 0.002 mmol), and tri(*o*-tolyl)phosphine (2.4 mg, 0.008 mmol) were added in a 0.5–2 mL microwave vial in air. The vial was capped and vacuumed for 20 min. It was refilled with nitrogen gas, and then, anhydrous chlorobenzene (1.6 mL) was added to the mixture. The reactor was degassed and refilled with nitrogen twice. The polymerization mixture was stirred and stepwise-heated to 100 °C (10 min), 140 °C (10 min), and 160 °C (40 min) in a microwave system. The polymer was end-capped by the addition of 2-bromothiophene (0.03 g, 0.177 mmol) and the mixture was further heated to 140 °C (20 min). Subsequently, 2-tributylstannyl thiophene (0.017 g, 0.047 mmol) was added and heated to 140 °C (20 min). The reaction mixture was cooled to room temperature and poured into a solution of methanol (300 mL) and 37% HCl (10 mL), and further purified by Soxhlet extraction with methanol, acetone, hexane, ethyl acetate, and chloroform. The chloroform fraction of **P-C4** was re-precipitated as methanol, filtered, and dried under vacuum. The other polymers were synthesized by following the same procedure as that employed for **P-C4**.

P(2DBDT-DTffBT)-C20, C4 (P-C4) (dark green solid, yield: 75%) ^{1}H NMR (400 MHz, $CDCl_3$, δ): 8.16–8.10 (br, 2H), 7.87–7.81 (br, 2H), 7.74–7.52 (br, 2H), 2.87–2.67 (br, 12H), 1.55–1.25 (br, 72H), 0.95–0.84 (br, 18H). Anal. calcn. (%) for $C_{80}H_{110}F_2N_2S_7$: C, 70.54; H, 8.14; F, 2.79; N, 2.06; S, 16.48; EA (%): C, 69.97; H, 8.01; N, 1.48; S, 16.79.

P(2DBDT-DTffBT)-C20, C6 (P-C6) (dark green solid, yield: 65%) ^{1}H NMR (400 MHz, $CDCl_3$, δ): 8.18–8.10 (br, 2H), 7.95–7.81 (br, 2H),

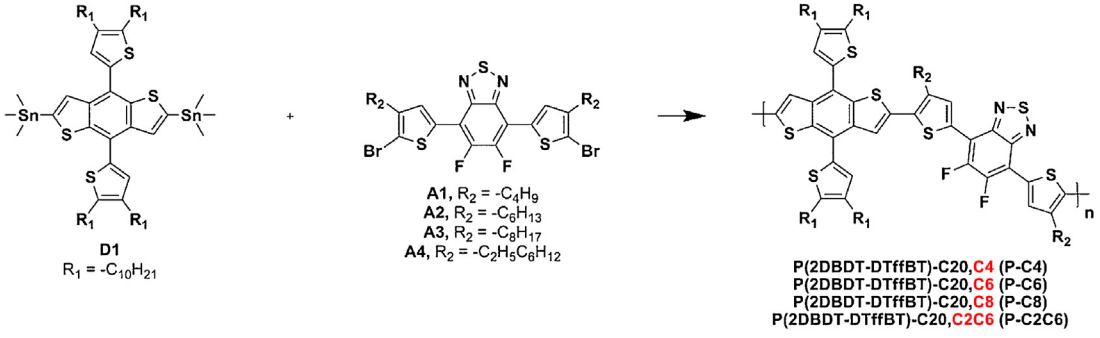

Scheme 1. Synthesis routes of P(2DBDT-DTffBT) series.

7.76–7.50 (br, 2H), 2.92–2.66 (br, 12H), 1.55–1.38 (br, 80H), 0.93–0.83 (br, 18H). Anal. calcn. (%) for $C_{84}H_{118}F_2N_2S_7$: C, 71.13; H, 8.39; F, 2.68; N, 1.98; S, 15.83; EA (%): C, 70.55; H, 8.20; N, 1.29; S, 15.97.

P(2DBDT-DTffBT)-C20, C8 (P-C8) (green solid, yield: 44%) ^{1}H NMR (400 MHz, $CDCl_3$, δ): 7.87–7.80 (br, 2H), 2.98–2.58 (br, 12H), 1.55–1.11 (br, 88H), 0.88 (br, 18H). Anal. calcn. (%) for $C_{88}H_{126}F_2N_2S_7$: C, 71.69; H, 8.61; F, 2.58; N, 1.90; S, 15.22; EA (%): C, 71.13; H, 8.39; N, 1.22; S, 15.23.

P(2DBDT-DTffBT)-C20, C2C6 (P-C2C6) (blue solid, yield: 25%) ^{1}H NMR (400 MHz, $CDCl_3$, δ): 8.19–8.15 (br, 2H), 7.86 (br, 2H), 7.36–7.20 (br, 2H), 2.96–2.60 (br, 12H), 1.76-1.67 (br, 8H), 1.57–1.10 (br, 80H), 0.95–0.86 (br, 18H). Anal. calcn. (%) for $C_{88}H_{126}F_2N_2S_7$: C 71.69; H, 8.61; F, 2.58; N, 1.90; S, 15.22; EA (%): C, 71.20; H, 8.44; N, 1.26; S, 15.45.

Results and discussion

Design and physical properties of materials

As shown in Scheme 1, 2DBDT, which offers high-performance combinations with most of the acceptor units of the polymer backbones, was selected as the donor unit (D1). In addition, four decyl side chains were introduced to 2DBDT to impart high solubility to the polymers. The DTffBT with diverse side chains, C4, C6, C8, and C2C6, were selected as the acceptor units (A1, A2, A3, and A4), respectively. The ffBT reveals stronger electron-withdrawing capabilities than non-substituted BT due to the two attached fluoro atoms, and its polymer has a more planar structure and deeper HOMO energy level than the BT polymers [23,30,47,53]. Lastly, the two variable alkyl side chain-substituted thiophene spacers (DT) were introduced to minimize the steric hindrance inside the D–A polymer backbones and optimize the properties of the polymer.

The designed polymers P-CmCn were synthesized through Stille coupling polymerization of the stannylated monomer (D1) and brominated monomers (A1, A2, A3, and A4) based on modification of the methods reported in the literature [57,61]. Once the polymerization was complete, the solution colors were similar to those observed in a photograph (SI, Fig. S10). The tendency of the bandgap of the polymer solutions to increase and its viscosity to decrease was observed as the length of the alkyl side chain increased from P-C4 to P-C2C6 and as the shape became bulkier from linear-type to branched-type. The resulting all polymers were purified by Soxhlet extraction with methanol (24 h), acetone (24 h), hexane (24 h), ethyl acetate (48 h), and chloroform (4 h), and the portions that dissolved in chloroform were re-precipitated as methanol. In the case of P-C2C6, it was completely extracted through Soxhlet purification with hexane (24 h) and re-precipitated as methanol. The polymers appeared dark green to blue solid in the order of P-C4, P-C6, P-C8, and P-C2C6. All the polymers are readily soluble in common organic solvents such as toluene, xylene, tetrahydrofuran, dichloromethane, chloroform, and chlorobenzene.

Table 1
Physical and thermal properties of polymers.

Polymer	Yield [%]	M_n[a] [kDa]	M_w[a] [kDa]	PDI[a]	T_d[b] [°C]	T_m[c] [°C]
P-C4	75.0	31.0	50.2	1.62	360	280
P-C6	65.0	25.1	39.7	1.58	357	256
P-C8[d]	44.0	13.5	19.9	1.47	323	212
P-C2C6[e]	25.0	8.9	14.5	1.63	313	–

[a] Determined by GPC in chloroform with polystyrene standard.
[b] Temperature corresponding to 5% weight loss based on initial weight.
[c] Temperature resulting in melting peaks.
[d] Chloroform fraction resulted in polymerization with the microwave system and minimized the molar ratios of the monomers.
[e] Hexane fraction resulted in polymerization with the thermal system and increased time.

The molecular weights of the polymers were determined through GPC by using chloroform as the eluent at room temperature. The results are shown in Table 1. Both P-C4 and P-C6 showed relatively high number-averaged molecular weights ($M_n \geq 25$ kDa) compared to P-C8 and P-C2C6 [62,63]. It has been reported that the molecular weights of the polymers would influence their photovoltaic properties by altering the aggregation behavior [64,65]. As the performance of the polymer largely depends on its molecular weight, the polymerization conditions were examined and modified to increase the degrees of polymerization of P-C8 and P-C2C6. The results on the molecular weight measurements for P-C8 and P-C2C6 under different polymerization conditions are presented in Fig. S11 and Table S1. The change in the conditions such as the polymerization system (microwave or thermal reactor), molar ratios of the monomers, and polymerization conditions (time/temperature, molar concentration, and catalysts/solvents) did not increase the degree of polymerization of both the polymers. Particularly, P-C2C6 showed a very low molecular weight, as the polymer was fully dissolved in hot hexane. As a result, 2DBDT-DTffBT-based polymers showed significantly different polymerization behaviors, even though the difference was only in the type of the alkyl side chains within the polymer backbones. This result suggests that polymer chain growth is largely affected by the length and shape of the alkyl side chains between the D and the A. It agrees with the previous studies of Lin et al. in that the steric hindrance in the main backbone largely affects the polymer chain growth [56–69]. This result will provide a useful platform for comparing the structure-property relationships arising from side chain variations.

The thermal properties of these polymers were analyzed by TGA and DSC, and the results are listed in Table 1. All the polymers showed good thermal stability up to 360 °C (temperature corresponding to 5% weight loss) and revealed endothermic peaks (with the exception of P-C2C6), as seen in Fig. S12. Particularly, because the polymers with the melting peaks (T_m) have good crystal structures, fine miscibility is expected during PCBM blending [70,71].

Optimizing the structure of 2DBDT-DTffBT through simple computational simulation

During the polymerization of general D–A conjugated polymers, it is crucial to investigate the possibility of intermolecular distortion due to steric hindrance in the main backbone for the continuous growth of the polymer chain [66–69]. Therefore, we examined the reasons for the lower degrees of polymerization of P-C8 and P-C2C6 under different polymerization conditions by using computational simulation.

We estimated the structures possible by calculating the dihedral angle-total energy according to the changes in the side chains (R_2) substituted into the thiophene spacer of the P (2DBDT-DTffBT) polymer, shown in Scheme 1. The dihedral angles and the possible conformations between the 3-alkyl side chain-substituted thiophene and the ffBT units were adapted from the analysis results of Lee et al. [27]. According to their dihedral angle calculations, the linkage between the 3-alkyl side chain substituted thiophene and ffBT shows two planar conformations (dihedral angles: 0° and 180°) due to intramolecular hydrogen bonding between the hydrogen in thiophene and the nitrogen in ffBT. Since the ffBT unit has an axisymmetric structure, either *cis* or *trans* structures with adjacent thiophenes are preferred. Thus, a minimum total of three energy conformations (*trans*/*trans*, *cis*/*trans*, and *cis*/*cis*) of the repeating polymer chain are possible.

In the case of the 2DBDT-DTffBT-based polymers investigated in this study, a total of six possible conformations are observed (marked as *up* or *dn* according to the direction of S of thiophene, including *trans(up,dn)*/*trans(up,dn)*, *trans(up,dn)*/*trans(dn,up)*, *cis(up)*/*trans(up,dn)*, *cis(up)*/*trans(dn,up)*, *cis(up)*/*cis(up)*, and *cis(up)*/*cis(dn)*); they can exhibit a total of 12 curvatures if all the overlap conformations are included (SI; Fig. S13). However, as shown in Fig. S14, the polymer chains can continuously grow only in the *trans*/*trans* conformation. The steric hindrance that can develop between the side chains of the polymer backbone would be higher in the order of *cis*/*cis*, *cis*/*trans*, and *trans*/*trans*, which suggests that the 2DBDT-DTffBT-based polymer chains prefer *trans*/*trans* structures [54,57,58,72,73]. Therefore, the 2DBDT-DTffBT-based polymer growth with *trans*/*trans* structures is significantly affected by the steric hindrance between the alkyl side chains that can develop in D–A systems.

Based on the above, we performed computational simulations using the software Gaussian 09 to investigate the direct steric hindrance in D–A systems due to the change in the alkyl side chains. Fig. 1(a) shows the calculation of the change in energy barrier according to the C3-C2-C2′-C3′ dihedral angle (α, 0° to 180°) of the 2-2′-bithiophene that has heterocycle rings as the flanked units. The definitions shown in Fig. 1(a) are as follows. The conformation names of the maximum or minimum points from 0° to 180° are in the order *cis*-planar, *cis*-local, TS (90°), *tans*-local, and *trans*-planar. ΔE_1 is the barrier between *cis*-planar and *cis*-local, ΔE_2 is the barrier between *cis*-local and the transition state, ΔE_3 is the barrier between the TS and *trans*-local, and ΔE_4 is the barrier between *trans*-local and *trans*-planar. Fig. 1(b) shows the 2DBDT-DTffBT structure in which the alkyl side chains are simplified into methyl groups to minimize the computational time and error. Fig. 1(c) shows the calculated minimized energy states according to the dihedral angle (α, 0° to 180°) scan of the structure of Fig. 1(b). Finally, Fig. 1(d) is a schematic depicting the optimized chemical structure of D–A according to dihedral angle based on the calculation results presented in Fig. 1(c). As shown in Fig. 1(c) and (d), two minimized energy states are shown between the 2DBDT-DTffBT-based D–A systems that were simplified into the methyl group, which suggest that the D–A has the *cis*-local minima at 20° (or 340°) and *trans*-local minima at 150° (or 210°). The ΔE_1, ΔE_2, ΔE_3, and ΔE_4 values were calculated as 0.065 kcal/mol, 2.352 kcal/mol, 2.401 kcal/mol, and 0.577 kcal/mol, respectively. The actual introduction of alkyl side chains in R_1 and R_2 of D–A will result in greater steric hindrance, which produces a shift in the direction of the arrow shown in Fig. 1(c) [66,74].

Optimizing the structure of 2DBDT-DTffBT through accurate computational simulation

To further investigate the steric hindrance developed in the D–A system according to the changes in the alkyl side chains (C_4, C_6, C_8, C_2C_6) of the 2DBDT-DTffBT block, computational simulations were performed using Gaussian 09 by introducing unsimplified alkyl side chains. For this purpose, one side of the thiophene of ffBT was removed to reduce the computing time. Fig. 2(a) shows the molecular structure and the *trans*/*cis*-planar examples used in this calculation, which are illustrated according to conformational change for better understanding. Fig. 2(b) presents the calculation results for the minimized energy states according to the dihedral angle (α, 0° to 180°) scans for the structures shown in Fig. 2(a), and Fig. 2 (c) is the normalized graph of Fig. 2(b). The results of Fig. 2(b) and (c) are summarized in Table 2.

As shown in Fig. 2(b) and (c), two minimized energy states are observed, which was the same as the result obtained from the introduction of the methyl group into the block, regardless of the types of alkyl side chains in 2DBDT-DTffBT. However, in the case of the methyl group substitution, the *cis*-local minima and *trans*-local minima are located at 20° and 150°, respectively, whereas, in the cases of P-C4, P-C6, and P-C8, they are observed at 30° and 140°, as shown in Fig. 2(b). This shift was greater in the case of P-C2C6 with the introduction of branched alkyl side chains, where the local minima were at 40° and 130°. As shown in Table 2, ΔE_1 increases in the order of 0.344 kcal/mol, 0.377 kcal/mol, 0.382 kcal/mol, and 0.791 kcal/mol, and ΔE_4 in the order 1.230 kcal/mol, 1.486 kcal/mol, 1.492 kcal/mol, and 1.684 kcal/mol as the number of alkyl side chains increased in the order P-C4, P-C6, P-C8, and P-C2C6. This increase in ΔE_1 and ΔE_4 is due to the increased steric hindrance between the alkyl side chain-substituted thiophene unit and the flanked 2DBDT unit [66,75–83]. This is because the longer the length of the alkyl side chains, from butyl, hexyl to octyl, the larger is the volume as the shape changes from linear-type to branched-type. In addition, as shown in Fig. 2(c), P-C2C6 reveals a decrease in the TS (90°) barrier of about 0.3 kcal/mol and a large local minima shift. This is due to the introduction of ethyl hexyl, which is a relatively bulky side chain group compared to the linear alkyl side chain, and results in an increase in the steric hindrance as a result

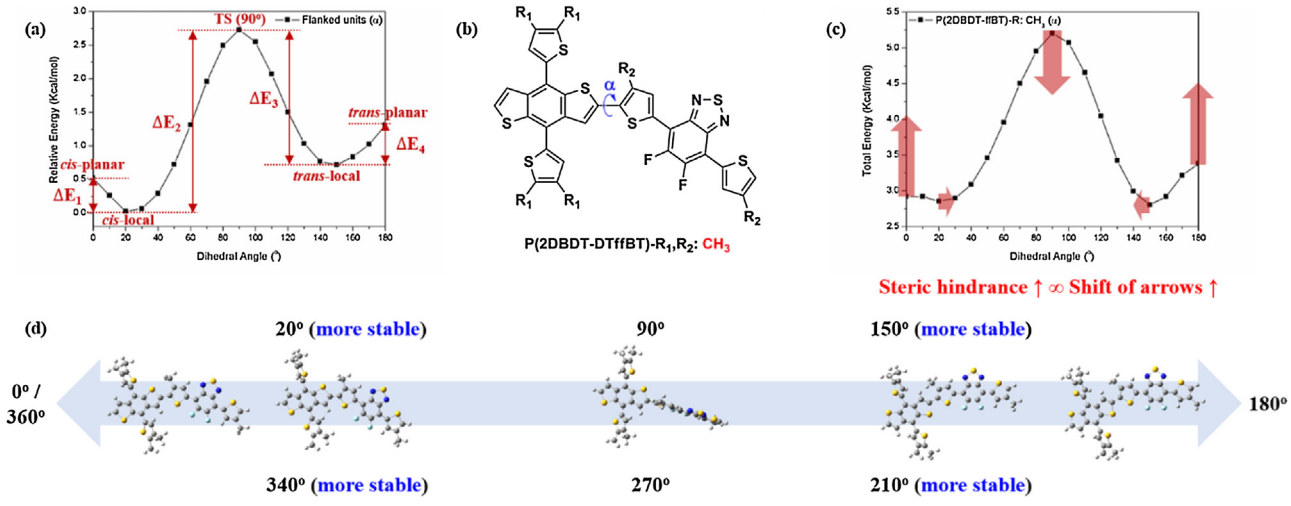

Fig. 1. (a) Definition of selected positions and energy barriers of substituted flanked units (*e.g.*, 2-2′-bithiophene); (b) the 2DBDT-DTffBT scheme with the alkyl side chains simplified; (c) the torsional potential of the structure shown in (b) obtained through dihedral angle scanning between the 2DBDT and DTffBT units; and (d) schematic illustration of the optimized chemical structure obtained from the results shown in (c).

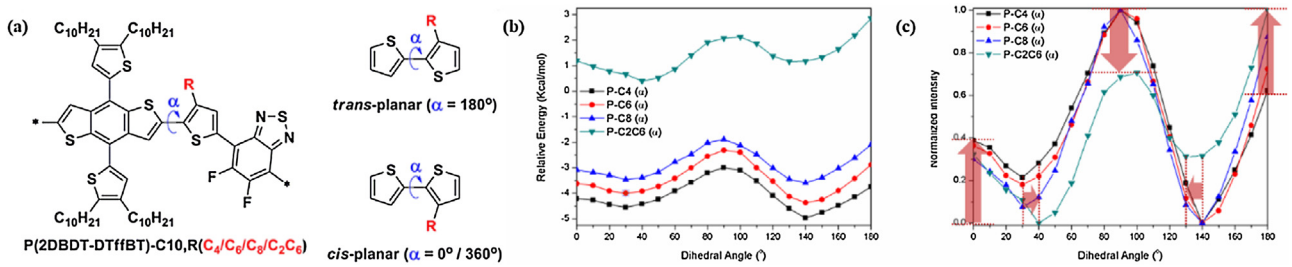

Fig. 2. (a) 2DBDT-DTffBT scheme without the simplification of alkyl side chains and a schematic example of their *trans*/*cis* conformation between flanked units; (b) the torsional potential of the structure shown in (a) obtained through dihedral angle scanning between the 2DBDT and DTffBT units; and (c) normalized graph of (b).

Table 2
Energy barriers of the different polymers (repeating unit, n = 1).

Polymer (n = 1)	ΔE_1[a] [kcal/mol]	ΔE_2[b] [kcal/mol]	ΔE_3[c] [kcal/mol]	ΔE_4[d] [kcal/mol]
P-C4	0.344	1.555	1.978	1.230
P-C6	0.377	1.682	2.052	1.486
P-C8	0.382	1.578	1.705	1.492
P-C2C6	0.791	1.732	0.966	1.684

[a] ΔE_1 is the barrier between *cis*-planar and *cis*-local.
[b] ΔE_2 is the barrier between *cis*-local and the transition state.
[c] ΔE_3 is the barrier between the transition state and *trans*-local.
[d] ΔE_4 is the barrier between *trans*-local and *trans*-planar.

of reduced planar structure and backbone conjugation [66,77,78,83]. The steric hindrance induced by the length and shape of the alkyl side chains in the D–A system can have a significant effect on the continuous chain growth of 2DBDT-DTffBT-based polymers. These results suggest that careful consideration and prediction of the introduction of suitable alkyl side chains in the design of D–A conjugated polymers is key to obtaining high-performance polymers.

DFT calculations

Fig. 3 shows the chemical structure of the polymers and the optimal geometry with the HOMO and LUMO surfaces of their conjugated backbones obtained from theoretical calculations based on DFT with the B3LYP/6-31G(d) basis set. For more accurate calculation and comparison, model compounds with n = 1

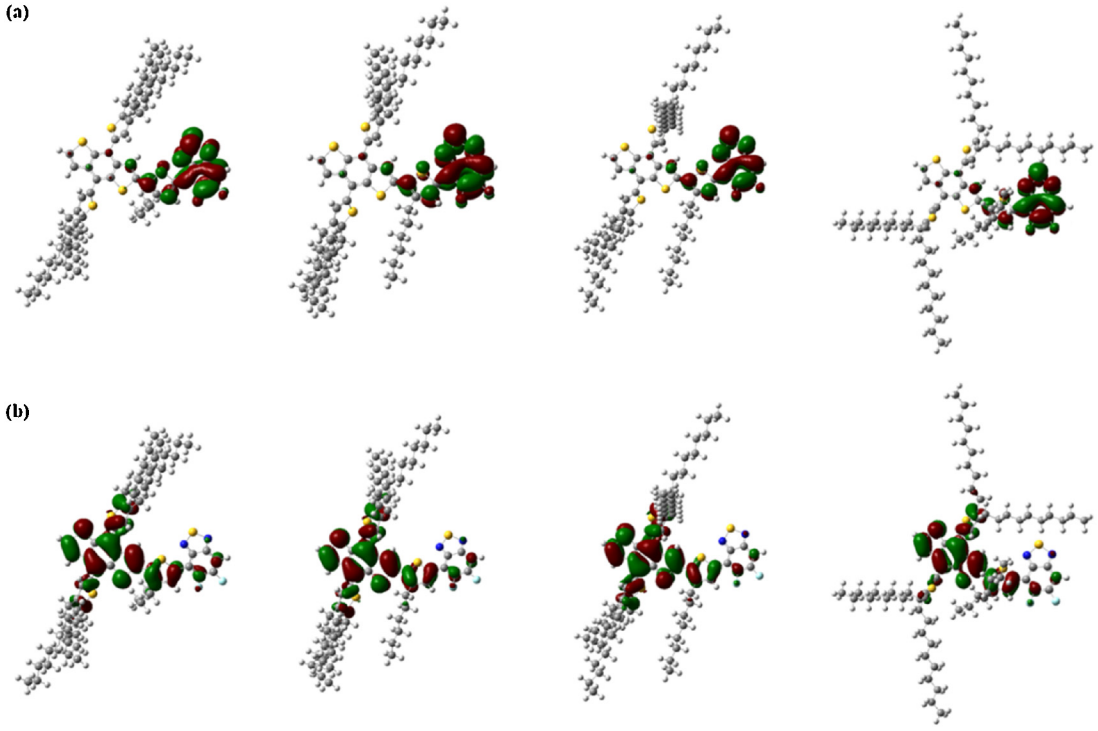

Fig. 3. DFT calculation data for P-C4, P-C6, P-C8, and P-C2C6 (repeating unit, n = 1): (a) LUMO and (b) HOMO energy levels.

structures, which refer to 2DBDT-DTffBT-based polymers having repeating units with unsimplified alkyl side chains, were employed. Then, one side of the thiophene of ffBT was also removed to reduce the computing time. As can be seen in Fig. 3(a) and (b), the LUMOs of the model compounds show electron clouds concentrated on the DTffBT units, indicating high electron mobility across the polymer backbones [84]. On the other hand, the electron density in the HOMOs is distributed along the entire polymer backbone, somewhat more intensely at the 2DBDT units and less so at the ffBT units. The electron density distributions of the different orbitals imply that internal charge transfers are possible in these D–A conjugated systems [72,73,85]. The DFT-calculated HOMO and LUMO energy levels and bandgaps of 2DBDT-DTffBT polymers with different alkyl side chains are summarized in Table 3. The HOMO energy level was slightly increased as the alkyl side chain length was increased, and deepened when the shape was changed from C8-linear to C2C6-branched [37,43,50,86]. However, the change in the bandgap was not significant because the change in the alkyl side chains did not significantly affect the electron cloud environment of the main backbones of 2DBDDT-DTffBT.

Optical and electrochemical properties

The optical absorptions of the polymers were investigated both in chloroform and thin films, as displayed in Fig. 4. Fig. 4(a) presents the averaged molar absorption coefficients of the polymers measured in different dilute solutions, whereas Fig. 4(b) and (c) are the UV–vis absorption spectra of the polymers in the solutions and thin films, respectively. Their optical and electrochemical properties are summarized in Table 4. All the polymers exhibit a high-energy absorption band in the region of 400–500 nm (0–2 absorption peak) corresponding to π–π^* transitions and a low-energy (500–720 nm, 0–1 and 0–0 absorption peaks; 0–0 peak of P-C2PC6 is none) absorption band corresponding to the strong ICT interaction between the D and A units [39,54,87]. The 0–0 peaks of the polymers in the solutions weakened as the length of the alkyl side chains increased or the shape changed from linear to branched. This tendency was similarly observed in the thin film states shown in Fig. 4(c), which suggests a decrease in the hole transport ability as a result of poorer crystallinity due to tilting between the D and the A in the polymer backbones [23,80]. From Fig. 4(a), Fig. S15, and the Beer–lambert equation ($A = \varepsilon bc$, where A: absorbance, ε: molar absorption coefficient of a dye, b: length of the light path, and c: concentration of the dye in solution), the ε values of P-C4, P-C6, P-C8, and P-C2C6 were calculated as 58074 $M^{-1}\,cm^{-1}$, 45470 $M^{-1}\,cm^{-1}$, 38147 $M^{-1}\,cm^{-1}$, and 12092 $M^{-1}\,cm^{-1}$ at λ_{max}, respectively. Because all the polymers except P-C2C6 revealed reasonable ε values of 30,000 or higher, greater harvesting of the solar photons and higher short circuit current densities (J_{sc}) were expected [82,83,86,88–90]. The reason for the decrease in ε from P-C4 to P-C2C6 is the decrease in the molecular weights [91–94]. As shown in Fig. 4(b) and (c), the main absorption peaks of the all polymers redshifted and showed broader absorptions in the thin film state than in the solution state. This is because ICT was strengthened by higher aggregation in the thin film state than in the solution state [74,79–81]. Therefore, the polymers P-C4, P-C6, P-C8, and P-C2C6 showed similar bandgaps of 1.72 eV, 1.73 eV, 1.74 eV, and 1.78 eV in the thin film state, respectively.

Table 3
Results of the DFT calculations of polymers (repeating unit, n = 1).

Polymer (n = 1)	HOMO [eV]	LUMO [eV]	E_g [eV]
P-C4	−5.046	−2.666	2.380
P-C6	−5.040	−2.653	2.387
P-C8	−5.022	−2.638	2.384
P-C2C6	−5.032	−2.657	2.375

To investigate the effect of alkyl side chains on the frontier energy levels of polymers, CV measurements were performed and the results are shown in Fig. 5(a). The HOMO and LUMO energy levels of the polymers were determined from the onset oxidation potential (E_{ox}^{onset}) and Eg–E_{HOMO} according to the following electrochemical equation: $E_{HOMO} = -4.8 - (E_{onset} - E_{1/2,ferrocene})$. The HOMO and LUMO energy levels were obtained and are listed in Table 4. The HOMO energy levels of the polymers slightly increased as the alkyl side chain length increased from C4, C6 to C8 [43,50]. This agreed well with the results of DFT calculations. On the other hand, P-C2C6 with the alkyl side chains changed from linear-type to branched-type showed largely decreased HOMO energy levels, which is due to the influence of the orbital–orbital overlap arising from the large tilting in the D–A system that is caused by the relatively bulky side chain of the ethyl hexyl group [33,86]. The HOMO energy levels of all the polymers must be lower than the air oxidation threshold of −5.27 eV in order for a material to exhibit oxidative stability [84]. The polymers of P-C4, P-C6, P-C8, and P-C2C6 showed superior oxidation stability, with HOMO energy levels of −5.55 eV, −5.53 eV, −5.50 eV, and −5.78 eV, which were lower than −5.27 eV. These deep HOMO energy levels of the polymers are expected to yield superior open circuit voltages for fullerene-blended PSCs [27,37,51]. Furthermore, the LUMO energy levels for P-C4, P-C6, P-C8, and P-C2C6 calculated by adding the optical bandgaps to the HOMO energy levels were −3.83 eV, −3.80 eV, −3.76 eV, and −4.00 eV, respectively, which allowed the smooth transfer of electrons due to there being only a 0.3 eV difference between these values and the LUMO energy level (−4.20 eV) of $PC_{71}BM$ [84]. Therefore, all the polymers except P-C2C6 are expected to reveal efficient electron transfer with $PC_{71}BM$. To make a clear comparison, the energy level diagrams of the polymers and $PC_{71}BM$ in fabricated inverted PSCs are summarized in Fig. 5(b).

Photovoltaic performance and PL analysis

To investigate the photovoltaic performance of the inverted device configuration ITO/ZnO (or ZnO + PFN)/Polymer:$PC_{71}BM$/MoO_3/Ag, the current density–voltage (J–V) curves and the EQE curves of the polymers were obtained, and are presented in Fig. 6 (a), (b) and Table 5, respectively. CB with DPE additive was chosen as the solvent for spin coating blend films. In particular, DPE was reported to induce optimal phase separation and heavy mixing between D and A in thick samples, resulting in the high performance of PSCs [57,95]. A series of devices with different polymer:$PC_{71}BM$ ratios (wt/wt), 1:1, 1:1.5, and 1:2 and different solvent conditions of DPE (1, 3, and 5 vol%) were fabricated in order to optimize the photovoltaic performance. The concentration of the all polymer blends with $PC_{71}BM$ ratio of 1:1.5 in CB and 3% DPE is optimized 1.5 wt%. Before spin coating the active layer, preheating (90 °C, 20 min) was carried out to obtain a fine morphology of the blend films. No post-treatment (annealing, solvent drying, *etc.*) was performed.

As shown in Fig. 6(a) and Table 5, the devices corresponding to P-C4, P-C6, and P-C8 exhibited their highest PCEs of 8.0%, 6.8%, and 4.6% at different thicknesses of 220 nm (P-C4, SI; Table S2), 180 nm, and 140 nm. In the case of P-C2C6, the fabricated device was not available due to its too low a molecular weight and too close a LUMO energy level compared to those of $PC_{71}BM$. The optimal thickness of the polymers was identified by alpha-step measurement of the regions of the cells with the highest PCEs. The V_{oc} and J_{sc} of the polymers were measured corresponding to the differences between the HOMO and LUMO energy levels measured by CV and the HOMO and LUMO energy levels of $PC_{71}BM$. The FFs for

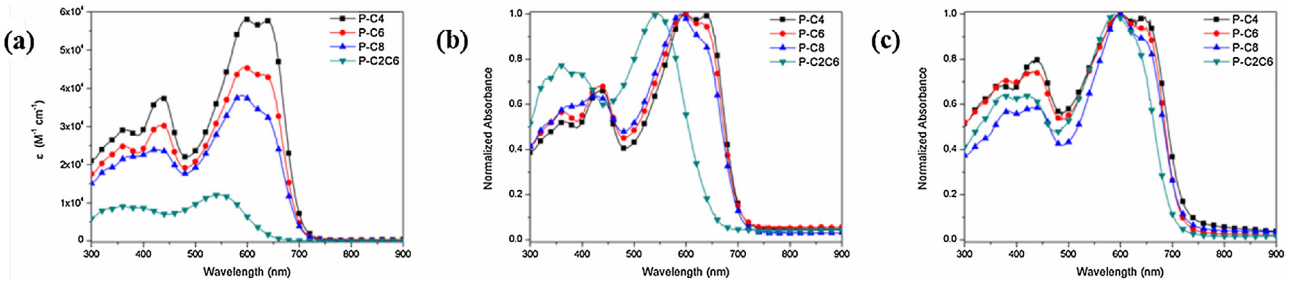

Fig. 4. UV–vis absorption spectra of P-C4, P-C6, P-C8, and P-C2C6: (a) Molar absorption coefficients in different dilute chloroform solutions; normalized absorbance (b) in solutions; and (c) of thin films on a quartz plate for the different chloroform solutions.

Table 4
Optical and electrochemical properties of polymers.

Polymer	UV–vis absorption			Cyclic voltammetry			
	Solution, λ^{solu}_{max} [nm]	Molar absorption coefficient, ε [$M^{-1}cm^{-1}$] at λ^{solu}_{max} [nm]	Film, λ^{Film}_{max} [nm]	$E_g^{opt,a}$[eV]	E_{ox}^{onset} [V]	E_{HOMO}^{b} [eV]	E_{LUMO}^{b} [eV]
P-C4	368, 438, 598, 638	58,074 (598)	373, 440, 597, 647	1.72	1.20	−5.55	−3.83
P-C6	363, 431, 595, 630	45,470 (595)	384, 432, 596, 641	1.73	1.18	−5.53	−3.80
P-C8	423, 592	38,147 (592)	382, 434, 599, 638	1.74	1.15	−5.50	−3.76
P-C2C6	359, 543	12,092 (543)	377, 418, 589	1.78	1.43	−5.78	−4.00

[a]Calculated from the intersection of the tangent on the low-energy edge of the absorption spectrum with the baseline.
[b]$E_{HOMO(orLUMO)} = -[E_{onset}(vs\ Ag/AgCl) - E_{1/2}(Fc/Fc^+ vs\ Ag/AgCl)^c] - 4.8\ eV$.
[c]$E_{1/2}(Fc/Fc^+ vs\ Ag/AgCl) = 0.45\ eV$ (measured data).

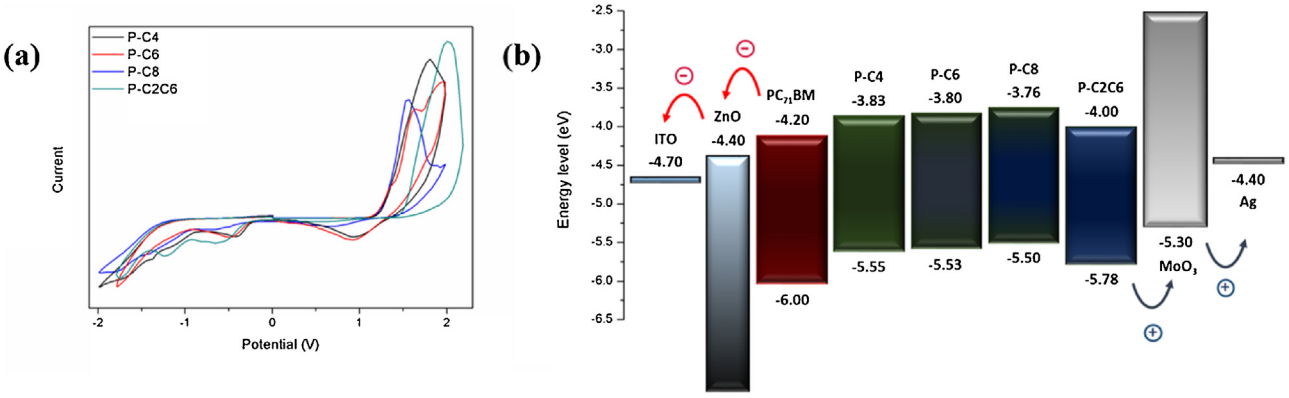

Fig. 5. (a) Cyclic voltammograms of P-C4, P-C6, P-C8, and P-C2C6 in thin films drop-casted on an ITO glass electrode at the scan rate of 50 mV/s; (b) energy level diagrams of the polymers and $PC_{71}BM$ in fabricated inverted PSCs.

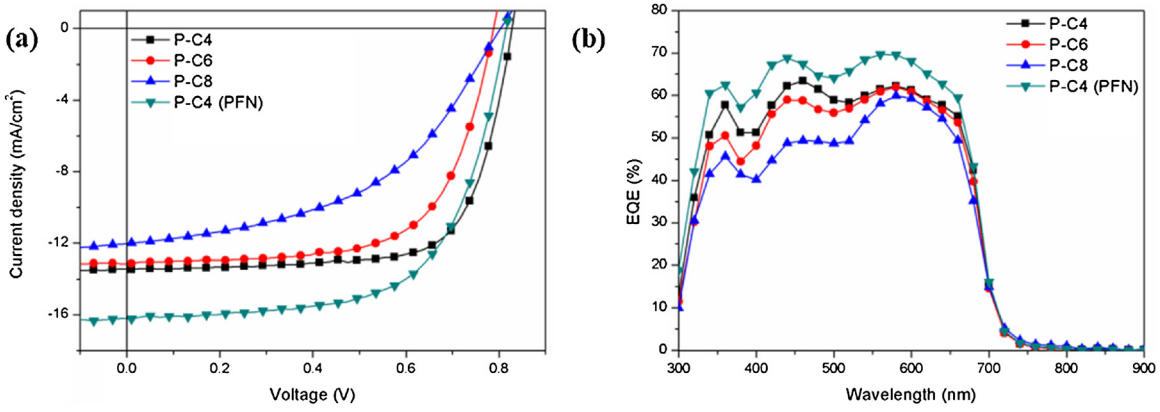

Fig. 6. (a) J–V curves and (b) EQE curves of polymer:$PC_{71}BM$ blends for inverted PSCs.

Table 5
Photovoltaic performances of PSCs based on polymers in inverted structures.

Conditions	Thickness [nm]	V_{oc} [V]	J_{sc} [mA/cm^2]	FF [%]	PCE_{max} [%]/ PCE_{ave}[a] [%]
P-C4:$PC_{71}BM$ = 1:1.5	220	0.818	13.5	72.4	8.0/7.8 ± 0.23
P-C6:$PC_{71}BM$ = 1:1.5	180	0.798	13.1	64.5	6.8/6.7 ± 0.08
P-C8:$PC_{71}BM$ = 1:1.5	140	0.798	12.0	48.0	4.6/4.5 ± 0.11
P-C4:$PC_{71}BM$ = 1:1.5 (PFN)	250	0.818	16.2	63.8	8.5/8.4 ± 0.12
P-C4:$PC_{71}BM$ = 1:1.5 (PFN)[b]	250	0.800	18.1	61.5	8.90

[a] The average PCE values were calculated for 10 independent cells.
[b] Independent certification results in Nano Convergence Practical Application Center (NCPC).

P-C4, P-C6, and P-C8 were 72.4%, 64.5% and 48.0%, respectively, showing large differences that were attributable to the difference in the molecular weights of the polymers. The molecular weight is known to have a considerable effect on the charge transport properties, so that as the molecular weight decreases, the intermolecular ordering and hole mobility decrease [1,3,55,56,64,68,91,93,94]. To further improve the photovoltaic performance of the P-C4 device, a ZnO + PFN hybrid interlayer was introduced as the cathode interface to boost electron extraction (P-C4 with PFN, SI; Table S3) [96]. As a result, a superior PCE of 8.5% after aging for 2 days was obtained, with enhanced J_{sc} of 16.2 mA/cm^2 for a 250 nm thick layer. After encapsulation, this cell was sent for certification to the Daegu Technopark Nano Convergence Practical Application Center (NCPC) in The Republic of Korea. The result of the test revealed a PCE of nearly 9%, as shown in Table 5. (SI; Fig. S16, S17) This test also evaluated the long-term stability at room temperature and 40% humidity for 824 h in air. The result showed that compared to the initial PCE of 8.3%, a value of 7.7% was observed after 824 h, indicating only about 8% decrease in the efficiency. This indicates excellent air stability of the polymer and fullerene blend [71,97]. Plus, the non-fullerene acceptor (ITIC-Th) was introduced as types of binary and ternary blends in order to enhance device performance of P-C4 [4–10]. The results of data were reasonable, but the effects of devices were less than the $PC_{71}BM$ blends. (P-C4 with ITIC-Th, SI: Fig. S18 and Table S4) The corresponding EQE curves of the devices for the optimal conditions of the polymer:$PC_{71}BM$ blends are shown in Fig. 6(b). All the devices exhibited a very broad response range 300–700 nm. The P-C4 and P-C6 devices, except P-C8, showed similar EQE profiles with high EQE responses in the high-energy region (400–500 nm), which might originate from the relatively highly matched $PC_{71}BM$ ratios in the active layers. The EQE responses of the three polymers were similar in the low-energy region (500–720 nm). This is because of high aggregation in the long-wavelength region even in the cases of P-C6 and P-C8, which have lower molecular weights than P-C4 [56]. Accordingly, similar J_{sc} values were obtained for both the devices of P-C4 and P-C6, as observed in Table 5. On the other hand, in the case of P-C8, because of its relatively low molecular weight, the EQE response decreased in the high-energy region [56,64,68,91]. In the case of P-C4 with PFN, a high J_{sc} value was obtained because of an enhancement of 5-10% in the EQE response across the entire absorption region.

To verify this increase in efficiency, we studied the fluorescence quenching of the polymers when mixed with $PC_{71}BM$ through PL measurement, the results of which are shown in Fig. 7. The PL spectra of the neat P-C4 film, the P-C4 blended film, and the P-C4 blend with PFN were obtained at the excitation wavelength of 598 nm. As shown in Fig. 7, the PL spectrum of the neat P-C4 film revealed maximum intensity at 746 nm, and the quenching efficiency at this point was 80% when it was blended with $PC_{71}BM$. The blend of P-C4 and PFN exhibited a quenching efficiency of 88%, indicating that the efficiency of exciton dissociation was high at the D–A interface [27]. In other words,

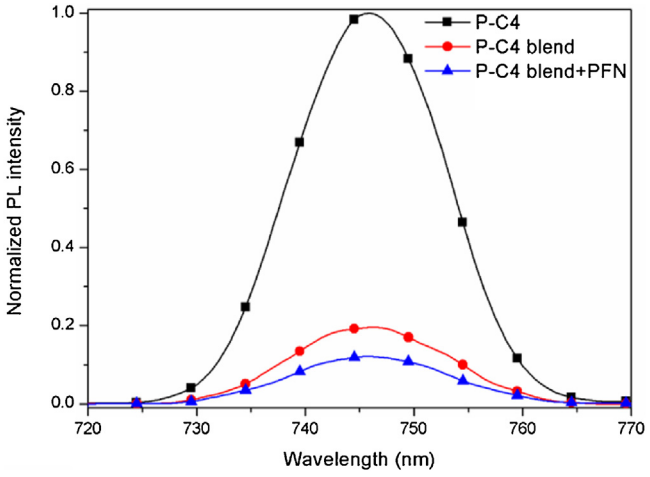

Fig. 7. Photoluminescence spectra of P-C4 pristine film, $PC_{71}BM$ blend film, and $PC_{71}BM$ film blended with PFN. The films were excited with 598 nm light. Each spectrum was corrected for the absorption of the film at the excitation wavelength.

increased exciton dissociation due to the introduction of PFN resulted in improved J_{sc} with effective charge transport characteristics [98,99].

Microstructural ordering and morphological characterization

The crystalline natures and molecular orientations of P-C4, P-C6, and P-C8 with various alkyl side chains were studied by XRD. The XRD patterns of the pristine polymers and polymer blends out-of-plane and in-plane are presented in Fig. 8. As shown in Fig. 8(a), in the out-of-plane direction, the pristine polymer films exhibit two peaks corresponding to (100) and (010) that are related to lamellar packing and π–π stacking. In the in-plane direction, the (010) peak of the polymers disappeared and only the (100) peak was observed in Fig. 8(b). Therefore, P-C4, P-C6, and P-C2C6 showed bimodal structural characteristics, displaying both edge-on and face-on orientations. The three polymer blends with $PC_{71}BM$ showed the (200) peak for the out-of-plane orientation, which indicated further enhanced lamellar packing. It also indicated that both vertical and horizontal charge transfers are possible in all the polymers due to the strong π–π stacking retained even after blending with $PC_{71}BM$ [54,63,72,83,87,88,93].

The lamellar and π–π stacking distances of the pristine polymers and polymer blends were calculated from the 2θ values by using Bragg's law ($\lambda = 2d\sin\theta$, Cu, λ: 1.541871 Å, d: distance), and their values are summarized in Table 6. The lamellar packing distances of pristine P-C4, P-C6, and P-C8 are 25.51 Å, 23.85 Å, and 24.60 Å, and the π–π stacking distances, as calculated, are 3.63 Å, 3.67 Å, and 3.69 Å, respectively. The interchain packing properties of the polymers were not significantly affected by the length of the

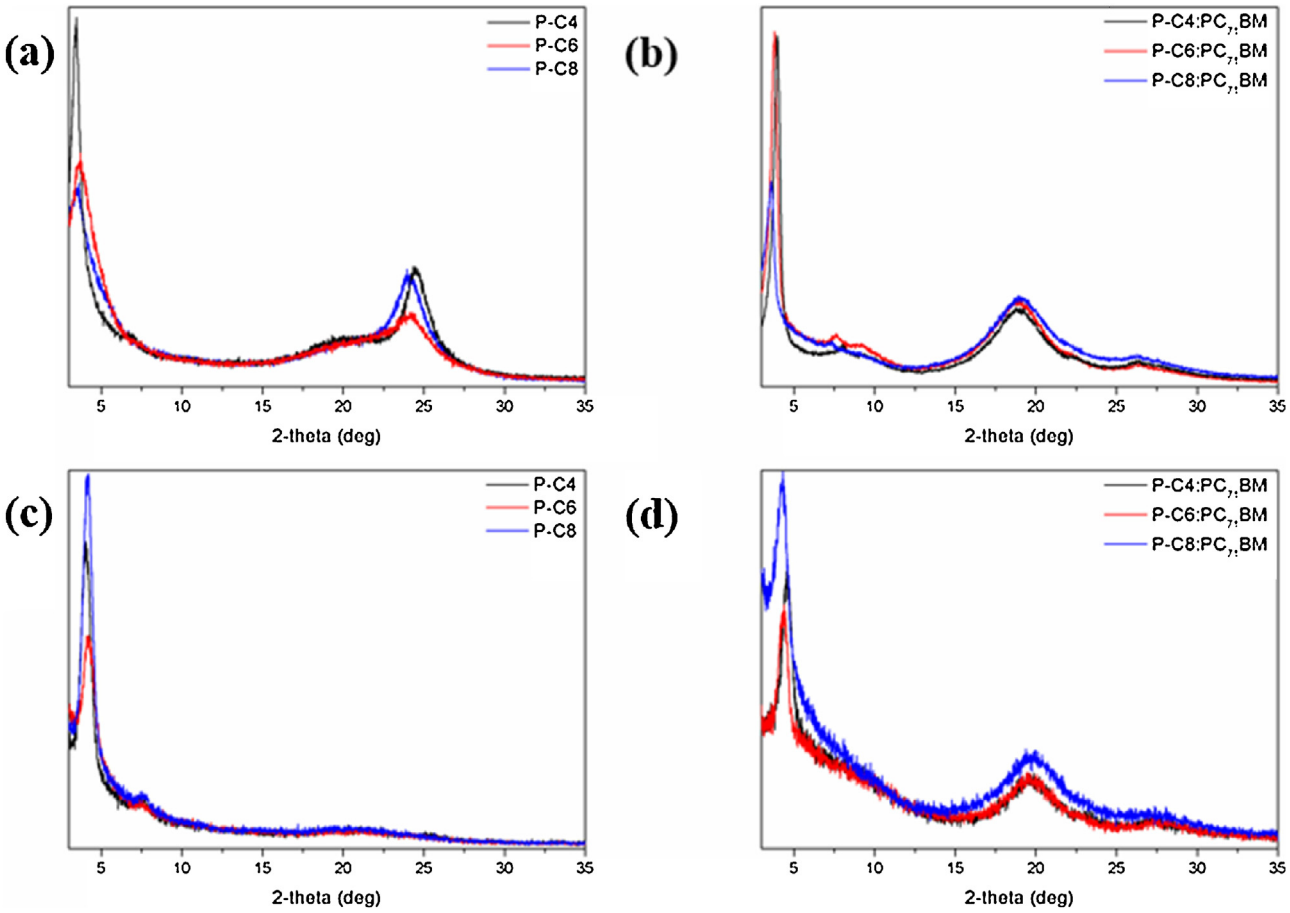

Fig. 8. XRD profiles of the pristine polymer films and the blend films: (a) pristine polymers and (b) blend films out-of-plane, (c) pristine polymers and (d) blend films in-plane.

Table 6
Molecular packing order obtained through XRD for different polymers.

Polymer	Conditions	2θ [°]/ d_{100} [Å]	2θ [°]/ d_{200} [Å]	2θ [°]/ d_{010} [Å]
P-C4	*Pristine*	3.46/25.51	–	24.50/3.63
	with $PC_{71}BM$	3.96/22.31	8.02/11.02	26.44/3.37
P-C6	*Pristine*	3.70/23.85	–	24.25/3.67
	with $PC_{71}BM$	3.80/23.25	7.61/11.62	26.38/3.38
P-C8	*Pristine*	3.59/24.60	–	24.12/3.69
	with $PC_{71}BM$	3.59/24.60	7.38/11.98	26.23/3.40

alkyl side chains because the lamellar packing order was determined by the long dodecyl side chains introduced into 2DBDT [28,40,41,45,47,54,56,77]. On the other hand, with respect to the π–π stacking characteristics, the planar structure of the polymer is inhibited and the π–π stacking distance increased by the disturbance of the intermolecular closed packing due to the introduction of bulky alkyl side chains [26,29,34,41,45,77]. The (100), (200), and (010) distances of the polymers blended with $PC_{71}BM$ are 22.31 Å, 11.02 Å, and 3.37 Å for P-C4, 23.25 Å, 11.62 Å, and 3.38 Å for P-C6, and 24.60 Å, 11.98 Å, and 3.40 Å for P-C8, respectively. All the polymers were blended with $PC_{71}BM$ to form

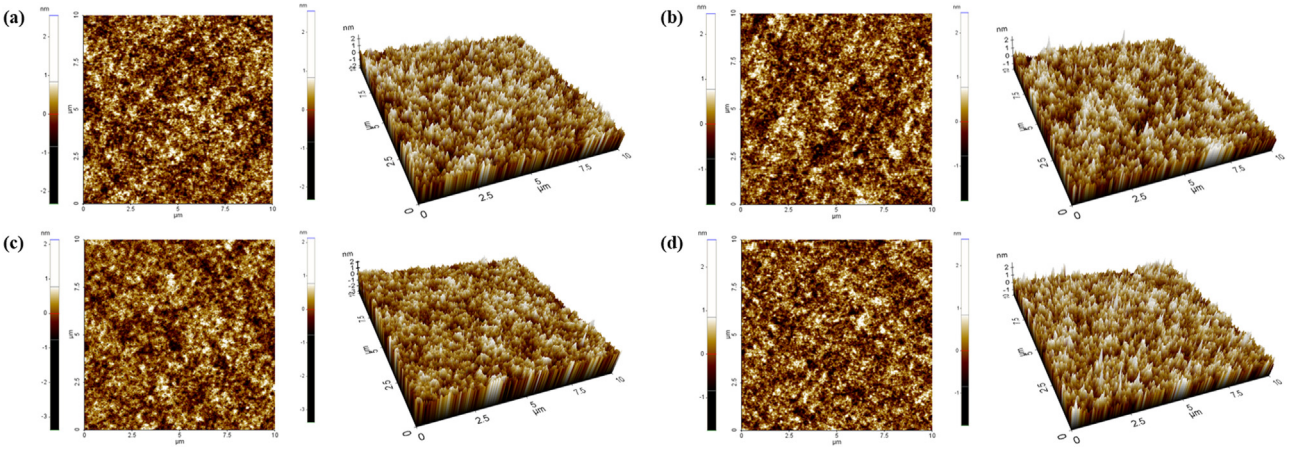

Fig. 9. AFM 2D and 3D topography images of polymer:$PC_{71}BM$ blend films under optimized conditions: (a) P-C4, (b) P-C6, (c) P-C8, and (d) P-C4 with PFN.

interpenetrating networks, resulting in stronger crystallinity, long-range ordering regularity, and short lamellar packing distance [36,49,50,54,56,63,65,86]. In addition, the π–π stacking of the polymer was maintained with shorter distance even after the blending with $PC_{71}BM$. This tendency reduced as the alkyl side chain length increased, and this was due to the low molecular weight and the steric hindrance caused by the introduction of bulky side chains in the D–A systems [33,37,43,50,54,86,93,94]. Conclusively, all the polymers showed efficient charge transfer because of improved lamellar packing and π–π stacking in the $PC_{71}BM$ blend, compared to the pristine form.

Tapping mode AFM was also carried out to investigate the phase-separated morphologies of the polymer:$PC_{71}BM$ blends corresponding to the best performance, and the results are shown in Fig. 9. As shown in the 2D and 3D topography images of the polymers in Fig. 9, the light and dark domains correspond to the aggregations of polymers and $PC_{71}BM$, respectively. All the films exhibit an interpenetrating feature with bi-continuous networks of appropriate domain sizes (≤20 nm) between the polymers and $PC_{71}BM$. Furthermore, smooth surfaces with RMS values of 0.540 nm for P-C4, 0.564 nm for P-C6, and 0.366 nm for P-C8 were obtained, as shown in Fig. 9 (a), (b), and (c). The RMS values of all the polymers were lower than 1.0 nm, and electron transfer between the polymers and $PC_{71}BM$ was efficient; this resulted in an increase in J_{sc}, which finally led to improvements in the device efficiency.

Finally, as seen from the 2D and 3D topography images in the cases of introducing PFN into the P-C4 blends, more microphases were found than in the case of the others, with nanofibril structures that increased the surface area being observed; these structures eventually boosted the electron movement and yielded high J_{sc} values, as shown in Fig. 9(d). Although a high RMS value of 0.700 nm was measured for P-C4 with PFN, this afforded the smallest aggregation size and allowed the system to reach the effective exciton diffusion length of PSCs [84,96].

Charge carrier transport properties

The electron and hole mobilities were measured to investigate the charge transport balance across the devices by using the SCLC method, as illustrated in Fig. 10. The structure of the electron-only devices was ITO/ZnO/polymer:$PC_{71}BM$/Al, while that of the hole-only devices was ITO/PEDOT:PSS/polymer:$PC_{71}BM$/MoO_3/Ag, and the Mott–Gurney space charge limited current formula (equation 1) was used to calculate the mobilities; the results are shown in Table 7. Here, μ stands for charge carrier mobility, ε_0 and ε_r are the dielectric constant of free-space and the permittivity of the active layer, respectively, and V and L represent the applied voltage and thickness of the semiconductor layer, respectively.

Table 7
Hole and electron mobilities of the active layer determined by using hole-only devices of ITO/PEDOT:PSS/polymer:$PC_{71}BM$/MoO_3/Ag and electron-only devices of ITO/ZnO/polymer:$PC_{71}BM$/Al, along with the use of the space charge current equation in the calculation.

Conditions	μ_h [cm^2/v·s]	μ_e [cm^2/v·s]	μ_e/μ_h
P-C4:$PC_{71}BM$	7.11×10^{-5}	5.28×10^{-3}	74.3
P-C6:$PC_{71}BM$	5.57×10^{-5}	5.24×10^{-3}	94.1
P-C8:$PC_{71}BM$	7.27×10^{-6}	5.20×10^{-5}	7.2
P-C4:$PC_{71}BM$ (PFN)	7.99×10^{-5}	8.85×10^{-3}	110.8

$$J = \left(\frac{9}{8}\right)\mu\varepsilon_0\varepsilon_r\left(\frac{V^2}{L^3}\right) \quad (1)$$

As the alkyl side chain length increased, the crystallinity and packing property decreased, and the hole and electron mobilities of the P-C4, P-C6, and P-C8 blends also decreased to values of $7.11 \times cm^2$/Vs, $5.57 \times cm^2$/Vs, and $7.27 \times cm^2$/V and $5.28 \times cm^2$/Vs, $5.24 \times cm^2$/Vs, and $5.20 \times cm^2$/Vs, respectively [1,54,68]. In particular, the balance ratios of the electron mobility to hole mobility for P-C4 and P-C6 were 74.3 and 94.1, respectively, which suggested imbalance. But the FFs of both the devices showed to 72.4% and 64.5%, respectively, due to the their fine morphology and reasonable molecular weights. On the other hand, P-C8 showed the best balance ratio of mobilities of 7.2, which was the closest to 1. However, its low molecular weight and decreased packing characteristics led to lower values of hole and electron mobilities of 10^{-6} and 10^{-5}, respectively. Thus, P-C8 exhibited the lowest FF of 48.0% [27,56,91].

The P-C4 blend with PFN showed increased hole and electron mobility values of $7.99 \times cm^2$/Vs and $8.85 \times cm^2$/Vs, respectively, resulting in a highest J_{sc} of 16.2 mA/cm^{-2} among the polymers [96]. However, the balance ratio of the mobilities increased to 110.8, resulting in a low FF of 63.8%. This trend agreed with the photovoltaic properties and film morphology discussed above [3,36,43,94].

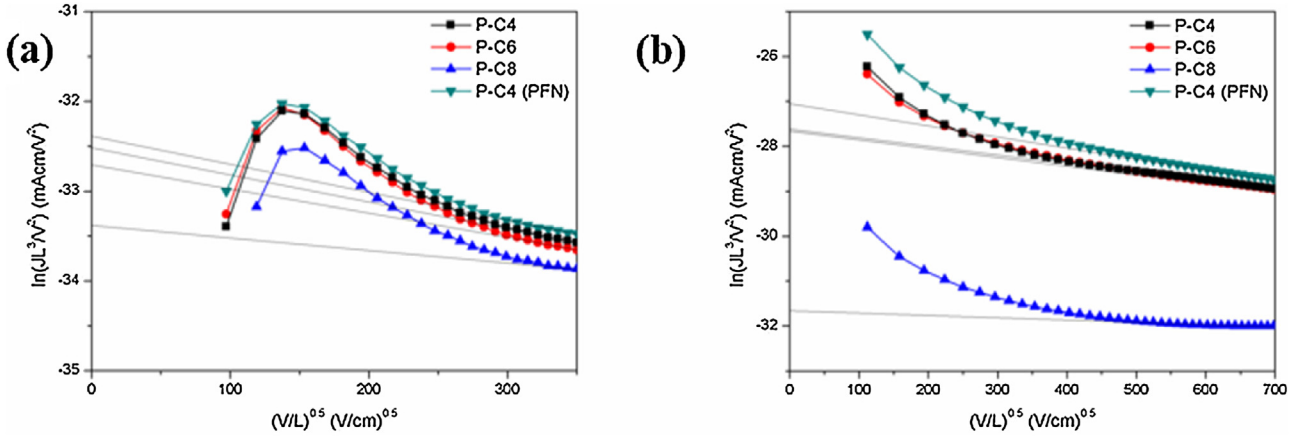

Fig. 10. SCLC, charge carrier mobility of optimized polymer blends for PSCs: (a) hole mobility, (b) electron mobility.

Conclusion

In this study, we designed and synthesized four donor polymers P-C4, P-C6, P-C8, and P-C2C6 based on 2DBDT-DTffBT (D–A) to obtain high performance with fullerene acceptor. The optimal geometries of the D–A conjugated polymers were calculated by tuning the alkyl side chains using the dihedral angle scan function, and their curvatures and the steric hindrance in the D–A units were also calculated with the software Gaussian 09. According to the theoretical calculation results, the relationship between the steric hindrance and the molecular weight of the P(2DBDT-DTffBT) series could be found to be related to the length and shape of the attached alkyl side chains. A greater increase in the alkyl side chain length and varying from linear to branched shape resulted in the molecular weights of P-C4, P-C6, P-C8, and P-C2C6 decreasing more significantly to 31.0 kDa, 25.1 kDa, 13.5 kDa, and 8.9 kDa, respectively, because of increased steric hindrance in the D–A units of the polymers. As a result, we report the best PCE of 8.9% with a P-C4:$PC_{71}BM$ blend that was obtained for a 250 nm thick active layer in the inverted device. The blended film had a bimodal structure with both edge-on and face-on orientations due to its high crystallinity and close packing order. These results demonstrate the great promise of D–A conjugated polymers and provide important scientific insights that facilitate further improvements in fullerene-based PSCs through material design and development.

Acknowledgments

This research was supported by the New and Renewable Energy Core Technology Program (No. 20153010140030) and the Human Resources Program in Energy Technology (No. 20174010201540) of Korea Institute of Energy Technology Evaluation and Planning (KETEP), which was granted financial resources by the Ministry of Trade, Industry and Energy, Republic of Korea.

Appendix A. Supplementary data

Supplementary data associated with this article can be found, in the online version, at https://doi.org/10.1016/j.jiec.2018.11.016.

References

[1] L. Lu, T. Zheng, Q. Wu, A.M. Schneider, D. Zhao, L. Yu, Chem. Rev. 115 (2015) 12666.
[2] P. Cheng, X. Zhan, Chem. Soc. Rev. 45 (2016) 2544.
[3] C. Duan, F. Huang, Y. Cao, Polym. Chem. 6 (2015) 8081.
[5] Z. Hu, F. Zhang, Q. An, M. Zhang, X. Ma, J. Wang, J. Zhang, J. Wang, ACS Energy Lett. 3 (2018) 555.
[6] Q. An, F. Zhang, J. Zhang, W. Tang, Z. Deng, B. Hu, Energy Environ. Sci. 9 (2016) 281.
[7] X. Ma, Y. Mi, F. Zhang, Q. An, M. Zhang, Z. Hu, X. Liu, J. Zhang, W. Tang, Adv. Energy Mater. 8 (2018) 1702854.
[8] M. Zhang, F. Zhang, Q. An, Q. Sun, W. Wang, J. Zhang, W. Tang, Nano Energy 22 (2016) 241.
[9] M. Zhang, F. Zhang, Q. An, Q. Sun, W. Wang, X. Ma, J. Zhang, W. Tang, J. Mater. Chem. A 5 (2017) 3589.
[10] M. Zhang, W. Gao, F. Zhang, Y. Mi, W. Wang, Q. An, J. Wang, X. Ma, J. Miao, Z. Hu, X. Liu, J. Zhang, C. Yang, Energy Environ. Sci. 11 (2018) 841.
[11] X. Ma, W. Gao, J. Yu, Q. An, M. Zhang, Z. Hu, J. Wang, W. Tang, C. Yang, F. Zhang, Energy Environ. Sci. 11 (2018) 2134.
[12] M. Zhang, Z. Xiao, W. Gao, Q. Liu, K. Jin, W. Wang, Y. Mi, Q. An, X. Ma, X. Liu, C. Yang, L. Ding, F. Zhang, Adv. Energy Mater. (2018) 1801968.
[13] Q. An, F. Zhang, L. Li, J. Wang, J. Zhang, L. Zhou, W. Tang, ACS Appl. Mater. Interfaces 6 (2014) 6537.
[14] Q. An, F. Zhang, L. Li, J. Wang, Q. Sun, J. Zhang, W. Tang, Z. Deng, ACS Appl. Mater. Interfaces 7 (2015) 3691.
[15] J. Yuan, L. Qiu, Z.G. Zhang, Y. Li, Y. Chen, Y. Zou, Nano Energy 30 (2016) 312.
[16] Z. Ji, X. Xu, G. Zhang, Y. Li, Q. Peng, Nano Energy 40 (2017) 214.
[17] Z. Ding, Z. Hao, B. Meng, Z. Xie, J. Liu, L. Dai, Nano Energy 15 (2015) 186.
[18] J. Zhao, Y. Li, G. Yang, K. Jiang, H. Lin, H. Ade, W. Ma, H. Yan, Nature Energy 1 (2016) 15027.
[19] W. Zhao, S. Li, H. Yao, S. Zhang, Y. Zhang, B. Yang, J. Hou, J. Am. Chem. Soc. 139 (2017) 7148.
[20] Q. Fan, Q. Zhu, Z. Xu, W. Su, J. Chen, J. Wu, X. Guo, W. Ma, M. Zhang, Y. Li, Nano Energy 48 (2018) 413.
[21] Q. Fan, W. Su, Y. Wang, B. Guo, Y. Jiang, X. Guo, F. Liu, T.P. Russell, M. Zhang, Y. Li, Sci. China Chem. 61 (2018) 531.
[22] S. Zhang, Y. Qin, J. Zhu, J. Hou, Adv. Mater. 30 (2018) 1800868.
[23] Y. Liu, J. Zhao, Z. Li, C. Mu, W. Ma, H. Hu, K. Jiang, H. Lin, H. Ade, H. Yan, Nat. Commun. 5 (2014) 5293.
[24] C. Sun, F. Pan, H. Bin, J. Zhang, L. Xue, B. Qiu, Z. Wei, Z.G. Zhang, Y. Li, Nat. Commun. 9 (2018) 1.
[25] J.H. Yun, H. Ahn, P. Lee, M.J. Ko, H.J. Son, Macromolecule 50 (2017) 7567.
[26] S. Tong, J. Yuan, C. Zhang, C. Wang, B. Liu, J. Shen, H. Xia, Y. Zou, H. Xie, J. Sun, S. Xiao, J. He, Y. Gao, J. Yang, Npj Flexible Electron. 2 (2018) 7.
[27] J. Lee, D.H. Sin, B. Moon, J. Shin, H.G. Kim, M. Kim, K. Cho, Energy Environ. Sci. 10 (2017) 247.
[28] H. Bin, Y. Yang, Z. Peng, L. Ye, J. Yao, L. Zhong, C. Sun, L. Gao, H. Huang, X. Li, B. Qiu, L. Xue, Z.G. Zhang, H. Ade, Y. Li, Adv. Energy Mater. 8 (2018) 1.
[29] Q. Peng, X. Liu, D. Su, G. Fu, J. Xu, L. Dai, Adv. Mater. 23 (2011) 4554.
[30] K. Feng, G. Yang, X. Xu, G. Zhang, H. Yan, O. Awartani, L. Ye, H. Ade, Y. Li, Q. Peng, Adv. Energy Mater. 8 (2018) 1602773.
[31] H. Yao, Y. Li, H. Hu, P.C.Y. Chow, S. Chen, J. Zhao, Z. Li, J.H. Carpenter, J.Y.L. Lai, G. Yang, Y. Liu, H. Lin, H. Ade, H. Yan, Adv. Energy Mater. 8 (2018) 1701895.
[32] X. Dong, H. Tian, Z. Xie, Y. Geng, F. Wang, Polym. Chem. 8 (2017) 421.
[33] L. Han, H. Jiang, D. Ouyang, W. Chen, T. Hu, J. Wang, S. Wen, M. Sun, R. Yang, Nano Energy 36 (2017) 110.
[34] Z. Luo, C. Sun, S. Chen, Z.G. Zhang, K. Wu, B. Qiu, C. Yang, Y. Li, C. Yang, Adv. Energy Mater. 8 (2018) 1.
[35] L. Yang, S. Zhang, C. He, J. Zhang, Y. Yang, J. Zhu, Y. Cui, W. Zhao, H. Zhang, Y. Zhang, Z. Wei, J. Hou, Chem. Mater. 30 (2018) 2129.
[36] Z. Wang, Z. Liu, L. Ning, M. Xiao, Y. Yi, Z. Cai, A. Sadhanala, G. Zhang, W. Chen, H. Sirringhaus, D. Zhang, Chem. Mater. 30 (2018) 3090.
[37] E. Al-Naamani, A. Gopal, M. Ide, I. Osaka, A. Saeki, ACS Appl. Mater. Interfaces 9 (2017) 37702.
[38] J. Liu, H. Choi, J.Y. Kim, C. Bailey, M. Durstock, L. Dai, Adv. Mater. 24 (2012) 538.
[39] L. Han, T. Hu, X. Bao, M. Qiu, W. Shen, M. Sun, W. Chen, R. Yang, J. Mater. Chem. A 3 (2015) 23587.
[40] C. Gu, D. Liu, J. Wang, Q. Niu, C. Gu, B. Shahid, B. Yu, H. Cong, R. Yang, J. Mater. Chem. A 6 (2018) 2371.
[41] M. He, M. Li, X. Dong, H. Tian, H. Tong, J. Liu, Z. Xie, Y. Geng, F. Wang, J. Mater. Chem. A 5 (2017) 20473.
[42] H.-Y. Chen, C.-W. Lin, C.-T. Chen, J. Golder, Y.-B. Lan, J.-K. Wang, Polym. Chem. 8 (2017) 3689.
[43] J.-H. Kim, S. Wood, J.B. Park, J. Wade, M. Song, S.C. Yoon, I.H. Jung, J.-S. Kim, D.-H. Hwang, Adv. Funct. Mater. 26 (2016) 1517.
[44] W. Li, K.H. Hendriks, A. Furlan, W.S.C. Roelofs, S.C.J. Meskers, M.M. Wienk, R.A.J. Janssen, Adv. Mater. 26 (2014) 1565.
[45] K.W. Song, T.H. Lee, E.J. Ko, K.H. Back, D.K. Moon, J. Polym. Sci. A: Polym. Chem. 52 (2014) 1028.
[46] M.-H. Choi, K.W. Song, D.K. Moon, Polym. Chem. 6 (2015) 2636.
[47] C. Duan, A. Furlan, J.J. Van Franeker, R.E.M. Willems, M.M. Wienk, R.A.J. Janssen, Adv. Mater. 27 (2015) 4461.
[48] C. Duan, R.E.M. Willems, J.J. van Franeker, B.J. Bruijnaers, M.M. Wienk, R.A.J. Janssen, J. Mater. Chem. A 4 (2016) 1855.
[49] C. Duan, K. Gao, F.J.M. Colberts, F. Liu, S.C.J. Meskers, M.M. Wienk, R.A.J. Janssen, Adv. Energy Mater. 7 (2017) 1700519.
[50] P. Liu, S. Dong, F. Liu, X. Hu, L. Liu, Y. Jin, S. Liu, X. Gong, T.P. Russell, F. Huang, Y. Cao, Adv. Funct. Mater. 25 (2015) 6458.
[51] Z. Yang, H. Chen, H. Wang, D. Mo, L. Liu, P. Chao, Y. Zhu, C. Liu, W. Chen, F. He, Polym. Chem. 9 (2018) 940.
[52] L. Ye, S. Zhang, L. Huo, M. Zhang, J. Hou, Acc. Chem. Res. 47 (2014) 1595.
[53] D. Liu, Q. Zhu, C. Gu, J. Wang, M. Qiu, W. Chen, X. Bao, M. Sun, R. Yang, Adv. Mater. 28 (2016) 8490.
[54] J. Lee, J.H. Kim, B. Moon, H.G. Kim, M. Kim, J. Shin, H. Hwang, K. Cho, Macromolecule 48 (2015) 1723.
[55] P. Deng, J. Yu, X. Yin, Y. Geng, B. Zhou, F. Zhang, W. Tang, Dyes Pigm. 138 (2017) 47.
[56] S. Fukuta, J. Seo, H. Lee, H. Kim, Y. Kim, M. Ree, T. Higashihara, Macromol. 50 (2017) 891.
[57] T.L. Nguyen, H. Choi, S.-J. Ko, M.A. Uddin, B. Walker, S. Yum, J.-E. Jeong, M.H. Yun, T.J. Shin, S. Hwang, J.Y. Kim, H.Y. Woo, Energy Environ. Sci. 7 (2014) 3040.
[58] A.C. Stuart, J.R. Tumbleston, H. Zhou, W. Li, S. Liu, H. Ade, W. You, J. Am. Chem. Soc. 135 (2013) 1806.
[59] V. Tamilavan, Y. Liu, J. Lee, Y.K. Jung, S.-M. Son, J.H. Jeong, S.H. Park, J. Mater. Chem. C 6 (2018) 4281.
[60] H. Yao, L. Ye, H. Zhang, S. Li, S. Zhang, J. Hou, Chem. Rev. 116 (2016) 7397.
[61] H. Hu, K. Jiang, G. Yang, J. Liu, Z. Li, H. Lin, Y. Liu, J. Zhao, J. Zhang, F. Huang, Y. Qu, W. Ma, H. Yan, J. Am. Chem. Soc. 137 (2015) 14149.
[62] Y. Yang, K. Mielczarek, A. Zakhidov, W. Hu, ACS Appl. Mater. Interfaces 8 (2016) 7300.
[63] T. Marszalek, M. Li, W. Pisula, Chem. Commun. 52 (2016) 10938.
[64] T. Vangerven, P. Verstappen, J. Drijkoningen, W. Dierckx, S. Himmelberger, A. Salleo, D. Vanderzande, W. Maes, J.V. Manca, Chem. Mater. 27 (2015) 3726.
[65] J. Lee, M. Kim, B. Kang, S.B. Jo, H.G. Kim, J. Shin, K. Cho, Adv. Energy Mater. 4 (2014) 1400087.
[66] T.-J. Lin, S.-T. Lin, Phys. Chem. Chem. Phys. 17 (2015) 4127.
[67] N.J. Hong, Y.S. Lee, J.H. Park, S.I. Na, J.C. Choe, K. Zong, Org. Electron. Phys. Mater. Appl. 42 (2017) 293.

[68] Y.Y. Lai, H.H. Chang, Y.Y. Lai, W.W. Liang, C.E. Tsai, Y.J. Cheng, Macromol. 48 (2015) 6994.
[69] C.-H. Lee, Y.-Y. Lai, J.-Y. Hsu, P.-K. Huang, Y.-J. Cheng, Chem. Sci. 8 (2017) 2942.
[70] J. Chen, L. Duan, M. Xiao, Q. Wang, B. Liu, H. Xia, R. Yang, W. Zhu, J. Mater. Chem. A 4 (2016) 4952.
[71] N. Li, J.D. Perea, T. Kassar, M. Richter, T. Heumueller, G.J. Matt, Y. Hou, N.S. Güldal, H. Chen, S. Chen, S. Langner, M. Berlinghof, T. Unruh, C.J. Brabec, Nat. Commun. 8 (2017) 14541.
[72] J. Shin, M. Kim, J. Lee, D. Sin, H.G. Kim, H. Hwang, K. Cho, RSC Adv. 5 (2015) 106044.
[73] W. Wang, G. Wang, J. Yang, J. Zhang, L. Chen, C. Weng, Z.G. Zhang, Y. Li, P. Shen, Chem. Phys. Lett. 672 (2017) 63.
[74] H. Wang, Y. Xu, X. Yu, R. Xing, J. Liu, Y. Han, Polymers 5 (2013) 1272.
[75] P.D. Homyak, Y. Liu, J.D. Harris, F. Liu, K.R. Carter, T.P. Russell, E.B. Coughlin, Macromol. 49 (2016) 3028.
[76] J. Wolf, F. Cruciani, A. El Labban, P.M. Beaujuge, Chem. Mater. 27 (2015) 4184.
[77] S. Tanaka, S.K.B. Rosli, K. Takada, N. Taniai, T. Yoshitomi, H. Ando, K. Matsumoto, RSC Adv. 7 (2017) 46874.
[78] O.G. Uzoh, P.T.A. Galek, S.L. Price, Phys. Chem. Chem. Phys. 17 (2015) 7936.
[79] D. Alberga, A. Perrier, I. Ciofini, G.F. Mangiatordi, G. Lattanzi, C. Adamo, Phys. Chem. Chem. Phys. 17 (2015) 18742.
[80] P. Guo, J. Sun, S. Sun, J. Li, J. Tong, C. Zhao, L. Zhu, P. Zhang, C. Yang, Y. Xia, RSC Adv. 7 (2017) 22845.
[81] D. Liu, L. Yang, Y. Wu, X. Wang, Y. Zeng, G. Han, H. Yao, S. Li, S. Zhang, Y. Zhang, Y. Yi, C. He, W. Ma, J. Hou, Chem. Mater. 30 (2018) 619.
[82] W. Zhong, J. Cui, B. Fan, L. Ying, Y. Wang, X. Wang, G. Zhang, X.F. Jiang, F. Huang, Y. Cao, Chem. Mater. 29 (2017) 8177.
[83] S. Zhang, B. Yang, D. Liu, H. Zhang, W. Zhao, Q. Wang, C. He, J. Hou, Macromol. 49 (2016) 120.
[84] S.J. Jeon, S.J. Nam, Y.W. Han, T.H. Lee, D.K. Moon, Polym. Chem. 8 (2017) 2979.
[85] Q. Fan, W. Su, X. Guo, X. Zhang, Z. Xu, B. Guo, L. Jiang, M. Zhang, Y. Li, J. Mater. Chem. A 5 (2017) 5106.
[86] L. Yang, H. Zhou, W. You, J. Phys. Chem. C 114 (2010) 16793.
[87] J. Wang, S. Wang, C. Duan, F.J.M. Colberts, J. Mai, X. Liu, X. Jia, X. Lu, R.A.J. Janssen, F. Huang, Y. Cao, Adv. Energy Mater. 7 (2017) 1702033.
[88] J.W. Jo, J.W. Jung, E.H. Jung, H. Ahn, T.J. Shin, W.H. Jo, Energy Environ. Sci. 8 (2015) 2427.
[89] J. Yuan, M.J. Ford, Y. Zhang, H. Dong, Z. Li, Y. Li, T.Q. Nguyen, G.C. Bazan, W. Ma, Chem. Mater. 29 (2017) 1758.
[90] Y. Jin, Z. Chen, S. Dong, N. Zheng, L. Ying, X.F. Jiang, F. Liu, F. Huang, Y. Cao, Adv. Mater. 28 (2016) 9811.
[91] C. Liu, K. Wang, X. Hu, Y. Yang, C.H. Hsu, W. Zhang, S. Xiao, X. Gong, Y. Cao, ACS Appl. Mater. Interfaces 5 (2013) 12163.
[92] Z. Xiao, K. Sun, J. Subbiah, T. Qin, S. Lu, B. Purushothaman, D.J. Jones, A.B. Holmes, W.W.H. Wong, Polym. Chem. 6 (2015) 2312.
[93] J. Gu, J. Yuan, W. Ma, Org. Electron. Phys. Mater. Appl. 34 (2016) 229.
[94] B. Fan, L. Ying, Z. Wang, B. He, X.-F. Jiang, F. Huang, Y. Cao, Energy Environ. Sci. 10 (2017) 1243.
[95] Y. Zheng, T. Goh, P. Fan, W. Shi, J. Yu, A.D. Taylor, ACS Appl. Mater. Interfaces 8 (2016) 15724.
[96] E.J. Lee, S.W. Heo, Y.W. Han, D.K. Moon, J. Mater. Chem. C 4 (2016) 2463.
[97] S. Holliday, R.S. Ashraf, A. Wadsworth, D. Baran, S.A. Yousaf, C.B. Nielsen, C.H. Tan, S.D. Dimitrov, Z. Shang, N. Gasparini, M. Alamoudi, F. Laquai, C.J. Brabec, A. Salleo, J.R. Durrant, I. McCulloch, Nat. Commun. 7 (2016) 11585.
[98] D. Liu, B. Yang, B. Jang, B. Xu, S. Zhang, C. He, H.Y. Woo, J. Hou, Energy Environ. Sci. 10 (2017) 546.
[99] H. Zhang, S. Li, B. Xu, H. Yao, B. Yang, J. Hou, J. Mater. Chem. A 4 (2016) 18043.